



1 **Sensitivity Studies of Four-Dimensional Local Ensemble**
2 **Transform Kalman Filter Coupled With WRF-Chem**
3 **Version 3.9.1 for Improving Particulate Matter Simulation**
4 **Accuracy**

5 Jianyu Lin^{1,2}, Tie Dai^{2*}, Lifang Sheng¹, Weihang Zhang¹,
6 Shangfei Hai³, Yawen Kong⁴

7 ¹ College of Oceanic and Atmospheric Sciences, Ocean University of China, Qingdao,
8 266100, China

9 ² State Key Laboratory of Numerical Modeling for Atmospheric Sciences and Geophysical
10 Fluid Dynamics, Institute of Atmospheric Physics, Chinese Academy of Sciences, Beijing,
11 China

12 ³ CMA Earth System Modeling and Prediction Centre, China Meteorological Administration
13 (CMA), Beijing 100081

14 ⁴ State Key Laboratory of Remote Sensing Science, Aerospace Information Research
15 Institute, Chinese Academy of Sciences, Beijing 100101, China

16 Correspondence: Tie Dai (daitie@mail.iap.ac.cn)

17 Abstract: Accurately simulate severe haze events through numerical models remains
18 challenging because of uncertainty in anthropogenic emissions and physical parameterizations
19 of particulate matter (PM_{2.5} and PM₁₀). In this study, a coupled WRF-Chem/four-dimension
20 local ensemble transform Kalman filter (4D-LETKF) data assimilation system has been
21 successfully developed to optimize particulate matter concentration by assimilating hourly
22 ground-based observations in winter over the Beijing-Tianjin-Hebei region and surrounding



23 provinces. The effectiveness of 4D-LETKF system and its sensitivity to ensemble member size
24 and length of assimilation window have been investigated. The promising results show that
25 significant improvements have been made by analysis in the simulation of particulate matter
26 during severe haze event. The assimilation reduces root mean square errors of $PM_{2.5}$ from 69.93
27 to $31.19 \mu\text{g m}^{-3}$ and of PM_{10} from 106.88 to $76.83 \mu\text{g m}^{-3}$. Smaller RMSEs and larger correlation
28 coefficients in the analysis of $PM_{2.5}$ and PM_{10} are observed across nearly all verification stations,
29 indicating that the 4D-LETKF assimilation optimizes the simulation of $PM_{2.5}$ and PM_{10}
30 concentration efficiently. Sensitivity experiments reveal that the combination of 48 hours of
31 assimilation window length and 40 ensemble members shows best performance for reproducing
32 severe haze event. In view of the performance of ensemble members, increasing ensemble
33 member size improves divergence among each forecasting member, facilitates the spread of
34 state vectors about $PM_{2.5}$ and PM_{10} information in the first guess, favors the variances between
35 each initial condition in the next assimilation cycle and leads to better simulation performance
36 both in severe and moderate haze events. This study advances our understanding about the
37 selection of basic parameters in the 4D-LETKF assimilation system and the performance of
38 ensemble simulation in a particulate matter polluted environment.

39 Key words: 4D-LETKF, severe haze simulation, ensemble member size, length of assimilation
40 window

41

42 1. Introduction

43 Although great progress about air pollution control has been made during recent years,
44 China is facing the highest levels of particulate matter in the world (van Donkelaar et al., 2016).



45 Particulate matter consists of $PM_{2.5}$ and PM_{10} , refers to particles with aerodynamic diameters
46 of less than 2.5 and 10 μm , respectively. High concentration of particulate matter is a major
47 factor for severe haze events (air quality index larger than 200) in the Beijing-Tianjin-Hebei
48 (BTH) region of China, especially during winter (Yan et al., 2016, Zhang et al., 2018).
49 Numerical models are considered to be useful tools for simulating haze events as for taking
50 complex physical and chemical mechanisms into account, but the uncertainty in emissions and
51 physical parameterizations still remain a significant barrier in improving the simulation
52 accuracy (Gao et al., 2017, Feng et al., 2018).

53 As an effective statistical approach, data assimilation is capable of improving the accuracy
54 of pollution simulations by limiting the performance of models. Lots of data assimilation
55 approaches have been applied to the atmospheric science, including three-dimension variation
56 (3D-Var) (Lorenz 1986; Parrish and Derber 1992; Sun et al., 2020), four-dimension variation
57 (4D-Var) (Huang et al. 2009; Benedetti et al., 2009), ensemble Kalman filter algorithms and
58 their variants (Evensen 1994; Whitaker and Hamill 2002; Miyazaki et al., 2012a), etc. Among
59 them, four-dimension local ensemble transform Kalman filter (4D-LETKF) has shown unique
60 characteristics in numerical simulation (Evensen, 2003, Kong et al., 2021). Firstly, derived from
61 finite forecasting members, the background error covariance matrix of 4D-LETKF features
62 flow-dependent characteristics, and the linear combinations of ensemble members produce
63 global analysis (Hunt et al., 2007). Secondly, the computational time for 4D-LETKF remains
64 robust as the observation numbers increase, exhibiting strong computational ability in the
65 parallel architecture when assimilate various measurements (Miyoshi et al., 2007; Hunt et al.,
66 2007, Dai et al., 2021). Lastly, 4D-LETKF can assimilate time slots of asynchronous



67 observations to optimize the current state within the assimilation window, which efficiently
68 improves the quality of pollution prediction (Evensen, 2003, Ott et al., 2004, Dai et al., 2019,
69 Cheng et al., 2019).

70 The characteristics of 4D-LETKF underscore the importance of ensemble member size
71 and length of assimilation window on its effectiveness. The ensemble member decides the
72 background error covariance matrix, representing the uncertainty in ensemble simulations
73 (Peng et al., 2017). 4D-LETKF considers approximate model trajectories by linear
74 combinations of the background ensemble trajectories. However, limited numbers of ensemble
75 members may bring about insufficient dispersion of ensemble systems (Hunt et al., 2004). In
76 addition, 4D-LETKF system can greatly improves the utilization rate of observations by
77 constrain the state variables in asynchronous hourly slot within the assimilation window. A
78 longer assimilation window efficiently reduces computational load by avoiding frequent
79 switches between state and forecast variables. But the trajectories over a long length of
80 assimilation window may diverge enough that linear combinations will not approximate the
81 model trajectories. Moreover, the model ensemble trajectory may not fit the observations well
82 over the entire interval with the presence of model errors (Dai et al., 2019). Many studies have
83 discussed the choice of these two parameters for ensemble Kalman filter algorithms and their
84 variants. When optimizing hourly aerosol fields by satellite observations, Cheng et al. (2019)
85 revealed that the forecast with a 24-hour assimilation window was comparable to those with 1-
86 hour, the root mean square error for AOD are 0.091 and 0.110, respectively, indicating the
87 weights determined at the end of the 24 hours assimilation window are valid to optimize the
88 ensemble trajectories. While Dai et al. (2019) proposed that over 80% of the hourly assimilation



89 efficiencies for the 1-hour assimilation window are higher than those with 6- or 24-hours in
90 4D-LETKF experiments, suggesting that assimilation efficiency decreases with the increase of
91 the assimilation window interval. These different opinions reveal that there is still a large
92 uncertainty about selection of parameters in 4D-LETKF assimilation system.

93 The accuracy simulation of severe haze events with air quality index (AQI) larger than 200
94 has been a challenging problem for a long time, posing severe threats to human daily life and
95 public health (Wang et al., 2014, Kong et al., 2021, Gao et al., 2017). Although 4D-LETKF has
96 unique advantages in computational efficiency and analysis, there are few researches
97 investigate the impacts of 4D-LETKF assimilation on pollutant simulation especially in severe
98 haze events, in addition, it is also imperative to explore the basic optimal combination of
99 assimilation parameters and its explanation in this method. Our major objectives are not only
100 to evaluate the performance of 4D-LETKF in reproducing particulate matter concentration
101 during severe haze event, but also to summarize the influence rules of ensemble size and
102 assimilation window length on particulate matter simulation, and explore whether these rules
103 are applicable to moderate haze event (air quality index smaller than 200) as well. The results
104 have great significance to verify and quantify the effect of 4D-LETKF assimilation on
105 numerical simulations of $PM_{2.5}$ and PM_{10} , subsequently provide a general rule for parameter
106 selection in the 4D-LETKF during severe haze event. Herein, we utilize 4D-LETKF system
107 which was coupled with Weather Research and Forecasting with Chemistry (WRF-Chem)
108 model to improve simulative skill of particulate matter among northern China during the winter
109 of 2020. Section 2 briefly introduces detail setting of WRF-Chem model, 4D-LETKF,
110 observations and numerical experiment designs. Section 3 compares the assimilation with those



111 in the prior simulation, summarizes and explains sensitivity rules for parametric selection, and
112 followed by a conclusion in Section 4 lastly.

113 2. Methodology

114 2.1 Configuration of the forecast model

115 In our implementation, the fully coupled “online” WRF-Chem version 3.9.1 is employed
116 as numeral forward model to describe the meteorological and chemical conditions
117 simultaneously, which fully considers extensive chemical transport processes including
118 advection, convection and sedimentation processes (Grell et al., 2005). The WRF-Chem model
119 is configured with two domains (d01 and d02), both using 100 (west–east) ×100 (south–north)
120 grid points, but with horizontal resolutions of 30 and 10 km, respectively. As shown in Figure
121 1(a), the d01 domain covers most part of East Asia, and the area under the blue shadow is the
122 d02 domain. The vertical grid contains 40 full sigma levels, extending from the surface to 50
123 hPa.

124 The initial and lateral boundary conditions of meteorological fields are derived from the
125 National Centers for Environmental Prediction Final (FNL) analysis data with a spatial
126 resolution of $1^\circ \times 1^\circ$ and temporal interval of 6 hours. A state-of-the-art and highly non-linear
127 gas-phase chemical mechanism Regional Atmospheric Chemistry Mechanism (RACM)
128 (Stockwell et al., 1997) is selected as gas phase mechanism, and Goddard Chemistry Aerosol
129 Radiation and Transport (GOCART) (Schwartz et al., 2012) is adopted as aerosol mechanism.
130 The parameterization scheme used in research is shown in Table 1.
131 Table 1. WRF-Chem parameterization scheme in this study.

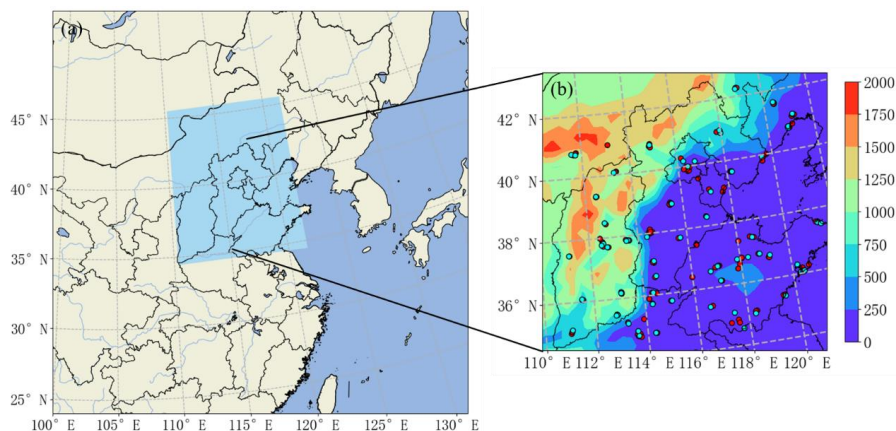
Parameterization	WRF-Chem option
------------------	-----------------



Microphysics	Morrison 2–moment Scheme (Morrison et al., 2019)
Longwave radiation	RRTMG Longwave Scheme (Iacono et al., 2008)
Shortwave radiation	RRTMG Shortwave Scheme (Iacono et al., 2008)
Planetary boundary layer	YSU Scheme (Hong et al., 2006)
Cumulus parameterization	Grell 3D Ensemble Scheme (Grell et al., 1993)
Land surface model	Noah (Tewari et al., 2004)

132

133 The anthropogenic emissions are obtained from the Multi-resolution Emission Inventory
134 for China compiled by Tsinghua University (MEIC, <http://www.meicmodel.org/>). The
135 inventory includes anthropogenic emissions from agriculture, industry, power, residential and
136 transportation sectors (Zheng et al., 2021). Inventory with a spatial resolution of $0.25^\circ \times 0.25^\circ$
137 and has been interpolated to match the simulation resolution. The biogenic emissions are
138 calculated online by Guenther scheme (Guenther et al. 1995). The $PM_{2.5}$, PM_{10} concentrations
139 output from WRF-Chem are linearly interpolated to site observations. The evaluation of
140 uncertainty in the emission inventory has been shown in previous research (Zhang et al., 2009).



141

142 Figure 1. (a) WRF-Chem model domains. (b) Location of assimilated and independent

143 verification observation sites with topography (units: m). The red and blue dot implies the

144 assimilated and independent verification observation site, respectively.

145 2.2 The 4D-LETKF algorithm and the state variables

146 The 4D-LETKF coupled with WRF-Chem Model is implemented to investigate the
147 influence of assimilation on particulate matter simulation in this research. In this section, we
148 introduce the 4D-LETKF algorithm and corresponding state variables briefly, more detailed
149 information can be found in Hunt et al. (2007). The LETKF features a flow-dependent
150 covariance matrix from ensemble simulation and determines the analysis ensemble mean \bar{x}^a
151 (a posteriori) according to the following formula:

$$152 \quad \bar{x}^a = \bar{x}^b + X^b \bar{w}^a$$

153 where \bar{x}^b and X^b denote ensemble mean of first guess and background ensemble
154 perturbations, respectively. The ensemble perturbation matrix X is calculated as $x(i) - \bar{x}$, $\{i =$
155 $1, 2, \dots, k\}$, which k represents the ensemble member size. The perturbation weight matrix \bar{w}^a
156 is the Kalman gain which linearly determines the increment between the analysis and the first
157 guess, and can be calculated as:



158
$$\bar{w}^a = \bar{P}^a (Y^b)^T R^{-1} (y^0 - \bar{y}^b)$$

159 where \bar{P}^a is analysis error covariance in ensemble space. y^0 and \bar{y}^b denote the
160 observations vector and ensemble mean background observations, respectively. Ensemble
161 mean background observations derived from applying observation vector to ensemble member
162 state vector $H(\bar{x}^b)$. The matrix R is the observation error covariance matrix. The matrix Y^b
163 represents ensemble background observation perturbations, whose i th columns is $y^{b(i)} - \bar{y}^b$,
164 $\{i = 1, 2, \dots, k\}$. \bar{P}^a can be obtained as:

165
$$\bar{P}^a = [(k - 1)I/\rho + Y^{bT} R^{-1} Y^b]^{-1}$$

166 where I denotes the identity matrix and k is ensemble member size. To prevent from filter
167 divergence, the multiplicative inflation factor ρ is set to 1.1 to inflate the analysis covariance
168 (Dai et al., 2019, Anderson, 2007). Analysis ensemble perturbations X^a is calculated by:

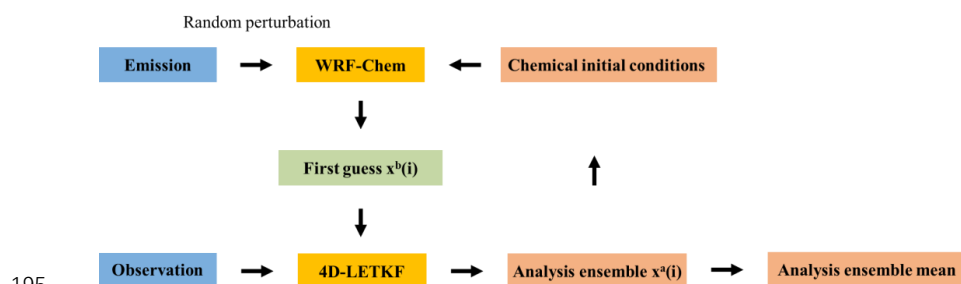
169
$$X_a = X_b [(k - 1)\bar{P}^a]^{1/2} = X^b W^a$$

170 Calculated by the sum of the \bar{x}^a and each of the columns of X_a , the ensemble analyses are
171 served as optimal initial conditions in each ensemble member to generate the first guess in the
172 next cycle.

173 Figure 2 is the flow chart of the WRF-Chem/4D-LETKF assimilation system applied in
174 our implementation. The system conducts these processes within each assimilation cycle. The
175 4D-LETKF generates a flow-dependent background error covariance matrix by ensemble
176 member. Given that the emissions inventory is an important source of uncertainty in simulation
177 (Pagowski and Grell, 2012), the research randomly perturbs anthropogenic emissions of PM,
178 black carbon (BC) and organic carbon (OC) in January for each member to create the ensemble
179 members, and the perturbation follows a log-normal distribution in the k -dimensional space.



180 The mean values of perturbations of $PM_{2.5}$, PM_{10} , BC and OC emissions are equal to 1, and the
181 variances of these emissions are set according to corresponding uncertainty in MEIC inventory
182 (Luo et al., 2023). Such ensemble anthropogenic emissions are perfect correlation in spatial and
183 temporal dimension and should not be regarded as overly restrictive (Schutgens et al., 2010).
184 This study only adds one times of perturbations into emissions at the first cycle of assimilation
185 to provide the information spread of particulate matter. The WRF-Chem/4D-LETKF system
186 propagates the ensemble forward simulation for the entire assimilation window time and
187 outputs the first guess fields at each hourly time slot. The ensemble mean of first guess (\bar{x}^b)
188 and background ensemble perturbations (X^b) can be obtained from ensemble member here.
189 Combining observation and observation operator, the innovation ($y^0 - \bar{y}^b$) and Y^b can be
190 obtained in each time slot. The perturbation weight matrix \bar{w}^a is valid within a relative short
191 assimilation window (e.g., 24 or 48 hours) (Hunt et al., 2004, Cheng et al., 2019). The analysis
192 ensemble derived from \bar{w}^a at the end of time slots will serve as chemical initial conditions for
193 the next assimilation window. As the cycle of assimilation proceed, a linear combination of
194 analysis ensemble is continuously obtained.



195 Figure 2. Flow chart of the WRF-Chem/4D-LETKF assimilation system for particulate

196 matter.

197 The ensemble Kalman filter generally encounters a spurious long-distance correlation



199 problem because of the limited numbers of ensemble members (Miyazaki et al., 2012a). To
200 avoid the problem above, it is necessary to apply observation localizations to filter observation
201 from a long distance. 4D-LETKF offers a flexible choice of observation localizations in
202 horizontal, vertical and temporal dimensions for each grid point (Cheng et al., 2019). In this
203 study, the horizontal localization factor is calculated as Gaussian function (Miyoshi et al., 2007),
204 which gradually reduces the effect of observation as the increasing departure from the analysis
205 grid:

$$206 \quad f(r) = \exp(-r^2/2\sigma^2)$$

207 Here, r represents physical distance from observation to analysis grid and σ represents
208 localization length. We limit the localization factor from 0 to 3.65 times the localization length
209 (Zhao et al., 2015), ignoring the observation beyond 3.65 times the localization length to the
210 analysis grid.

211 The selection of the state variables depends on the generative mechanism of aerosol. As a
212 result, 16 kinds of WRF-Chem/GOCART aerosol variables are treated as state variables. For
213 the $PM_{2.5}$ observations, the observation operator is described as:

$$214 \quad y_{PM_{2.5}}^f = \rho_d [P_{2.5} + 1.375S + 1.8(OC_1 + OC_2) \\ 215 \quad + BC_1 + BC_2 + D_1 + 0.286D_2 + S_1 + 0.942S_2]$$

216 where ρ_d present the dry-air density, $P_{2.5}$ is the fine unspecified aerosol contributions,
217 S represents sulfate, OC_1 and OC_2 are hydrophobic and hydrophilic organic carbon, respectively.
218 BC_1 and BC_2 are hydrophobic and hydrophilic black carbon, D_1 and D_2 are dusts with effective
219 radii of 0.5 and 1.4 μm , and S_1 and S_2 are sea salts with effective radii of 0.3 and 1.0 μm ,
220 respectively (Peng et al., 2018).



221 Similarly, the observation operator for PM_{10} is shown as below:

$$222 \quad y_{PM_{10}}^f = \rho_d [P_{10} + P_{2.5} + 1.375S + 1.8(OC_1 + OC_2) \\ 223 \quad + BC_1 + BC_2 + D_1 + 0.286D_2 + D_3 + 0.87D_4 + S_1 + 0.942S_2 + S_3]$$

224 where P_{10} is coarse unspecified aerosol contributions, D_3 and D_4 are dusts with
225 effective radii of 2.4 and 4.5 μm . S_3 is sea salt with effective radii of 3.2 μm . Therefore, the
226 simulated $PM_{10-2.5}$ is:

$$227 \quad y_{PM_{10-2.5}}^f = \rho_d [P_{10} + D_3 + 0.87D_4 + S_3]$$

228 In this research, $y_{PM_{10-2.5}}^o$ calculated by $y_{PM_{10}}^o - y_{PM_{2.5}}^o$ is used to analyze state variables
229 including D_5 and S_4 , which are dust with effective radii of 8 μm and sea salt with effective
230 radii of 7.5 μm , respectively.

231 2.3 Site observation data and errors

232 Ground-based observation features high temporal resolution, which can capture variation
233 of pollution concentration on an hourly scale at the bottom of the troposphere, providing
234 continuous and reliable observation. The quality-assure and quality-controlled hourly
235 observation data of $PM_{2.5}$ and PM_{10} are used to explore the influence of 4D-LETKF assimilation
236 in this research. The pollution data was obtained from China National Environmental
237 Monitoring Center (<http://106.37.208.233:20035/>). As the research primarily focuses on the
238 BTH region, the assimilation and verification sites are mainly located in the BTH region and
239 neighboring provinces, primarily located in urban and suburban areas. In order to obtain more
240 reliable observation data, the quality control of observation data in this study includes hourly
241 observation of default value and extreme value detection. First, during the haze period, if the
242 number of missing values for either type of pollutant at one site exceeds 24 hours, this site is



243 considered to have a certain uncertainty on observation quality, and data will not be assimilated.
244 Second, for each kind of observation in different station, the hourly observation outside the
245 range of $m \pm 3\sigma$ will not be assimilated, where the m and σ denote the mean value and standard
246 deviation of daily time series, respectively. When selecting assimilation and verification sites,
247 spatial distribution uniformity is ensured for better assimilation performance, consequently,
248 those sites are randomly selected. Finally, 127 assimilation sites and 69 verification sites in the
249 BTH region and surrounding province are selected (Figure 1b). It can be seen that the
250 assimilation and verification sites have a relatively uniform spatial distribution.

251 The observation error covariance matrix (R) is assumed to be diagonal, implying that
252 observational errors among each pollution species are uncorrelated. The observation error (r)
253 consists of measurement error (ε_0) and representation error (ε_r):

$$254 \quad r = \sqrt{\varepsilon_0^2 + \varepsilon_r^2}$$

255 The measurement error ε_0 is defined as:

$$256 \quad \varepsilon_0 = \text{ermax} + 0.0075 * \Pi_0$$

257 where ermax is the base error, which is set to be 1 for $\text{PM}_{2.5}$, and PM_{10} (Chen et al., 2019a),
258 Π_0 denotes the observation of concentration. Produced by observation operator,
259 representativeness errors can be calculated by the formula (Elbern et al., 2007):

$$260 \quad \varepsilon_r = \gamma \varepsilon_0 \sqrt{\Delta l / L}$$

261 γ is tunable scaling factor and 0.5 is set for γ , Δl is the spatial resolution of gridding (30 km
262 and 10km for $d01$ and $d02$, respectively), L depends on station location, which denotes the
263 range that an observation can reflect, here L is 2 km for calculation.

264 Meteorological data were collected from National Climatic Data Center



265 (<https://www.ncei.noaa.gov/>), which provides hourly air temperature, dew point, and
266 windspeed data. The observational meteorological data are used to validate the performance of
267 simulations in this study.

268 2.4 Experiment design

269 A series of control and data assimilation experiments during severe and moderate haze
270 events, as listed in Table 2, have been carried out to achieve our major objective. The control
271 experiments refer to numerical experiments without data assimilation. The Severe-FR
272 experiment with 48 hours spin up time is performed firstly to quantify the necessity of adjusting
273 particulate matter concentration during severe haze event. Severe-FR-24h, Severe-FR-48h, and
274 Severe-FR-72h accompany with restart every 24, 48, and 72 hours respectively and update
275 meteorological boundary conditions. Except Severe-FR, the rest of the experiments all have 72
276 hours of free run as the basic chemical initial condition input to balance the pollutant
277 concentration, and accompany 24 hours of spin up time at the beginning of each restart or
278 assimilation cycle. Since the effectiveness of 4D-LETKF is highly related with ensemble
279 member size and length of assimilation window (Rubin et al., 2016), the sensitivity analysis is
280 employed to investigate the influence from two parameters on assimilation effect (Kong et al.,
281 2023). The selection of assimilation parameters for the sensitivity experiments includes 20, 40
282 and 60 for ensemble members, and 24, 48 and 72 hours for the length of assimilation window
283 empirically (Kong et al., 2021, Dai et al., 2021). All sensitivity experiments use identical WRF-
284 Chem physical parameterizations, anthropogenic emission and random perturbations. Through
285 the comparison between all assimilation experiments, the influence rules of 4D-LETKF
286 assimilation on the simulation of particulate matter in severe haze can be retrieved. Lastly,



287 aiming to determinate the applicable range of obtained influence rules above, two assimilation
 288 experiments in a moderate haze event are performed to validate whether the rules are also
 289 suitable to a less-polluted environment. The detail reasons for selection of parameters will be
 290 fully described in the next section.

291 Table 2. design of numerical experiments in this research.

	Experiment	Design of simulation
Control experiments	Severe-FR	Free run experiment in severe haze event and without restart in integration process.
	Severe-FR-24h	Free run experiment in severe haze event and with
	Severe-FR-48h	restart every 24, 48 and 72 hours, provide
	Severe-FR-72h	deterministic simulation corresponding to data assimilation experiment.
	Moderate-FR-48h	Free run experiment in moderate haze events and with restart every 48 hours, provide deterministic simulation corresponding to data assimilation experiment.
Data assimilation experiments in severe haze event	Severe-20m-24h	Assimilation experiment in severe haze event with
	Severe-20m-48h	20 ensemble members and 24, 48, 72 hours of
	Severe-20m-72h	assimilation window length respectively.
	Severe-40m-24h	Assimilation experiment in severe haze event with
	Severe-40m-48h	40 ensemble members and 24, 48, 72 hours of
	Severe-40m-72h	assimilation window length respectively.



	Severe-60m-24h	Assimilation experiment in severe haze event with
	Severe-60m-48h	60 ensemble members and 24, 48, 72 hours of
	Severe-60m-72h	assimilation window length respectively.

Data	Moderate-20m-48h	Assimilation experiment in moderate haze event
assimilation	Moderate-40m-48h	with 20 and 40 ensemble members combine with 48
experiments in		hours of assimilation window length.
moderate haze		
event		

292 Root mean square error (RMSE), mean errors (BIAS), mean absolute error (MAE) and
293 correlation coefficient are calculated in this study to evaluate the performance of each numerical
294 experiment. The assimilation efficiency (AE) for estimating the data assimilation performance
295 is also calculated from the formulation below (Yumimoto and Takemura, 2011):

296
$$AE = \frac{RMSE^f - RMSE^a}{RMSE^f} \times 100\%$$

297 where $RMSE^f$ and $RMSE^a$ is RMSE with and without assimilation, respectively. According
298 to the definition, if AE is positive, it means that RMSE has decreased due to assimilation effect.

299 When AE is equal to 1, RMSE in analysis completely disappears, and analysis is equal to
300 observation.

301 3. Results

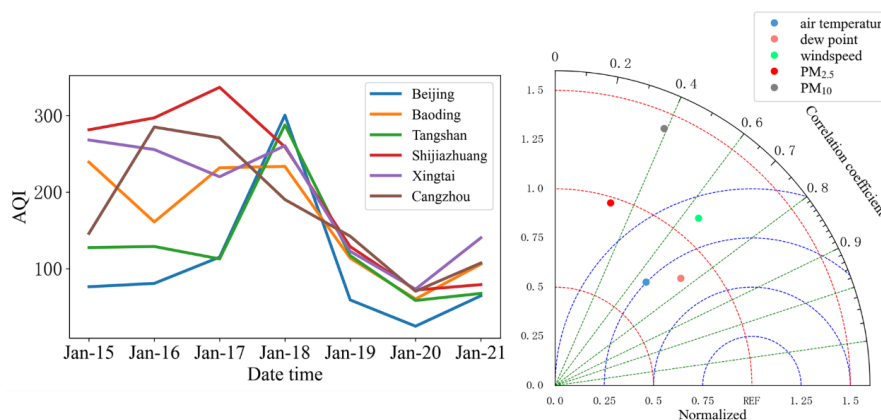
302 3.1 Comparison of the analysis with control experiment

303 3.1.1 The simulation of the severe haze event in BTH

304 It is essential to discuss the basic evolution of pollutant and the necessity of pollutant data
305 assimilation in severe haze event before conducting the assimilation experiments. The severe



306 haze event selected in this study occurred from 00:00 UTC 15 January 2020 to 00:00 UTC 21.
307 Figure 3(a) shows the temporal variation of air quality index at the six sites among BTH region
308 during the investigated period. The peak AQI mainly appeared on 18 January, and then rapidly
309 decreased on 19 and 20 January. The temporal averaged of AQI have exceeded 200, with
310 particulate matter identified as the primary pollutant. Fig. 3(b) provides the correlation
311 coefficients and standardized standard deviations of five parameters from Severe-FR against
312 observations. Meteorological variables including air temperature, dew point temperature and
313 wind speed are well simulated when compared with $PM_{2.5}$ and PM_{10} . The correlation
314 coefficients of meteorological factors are larger than 0.6, while that of pollutant concentrations
315 are below 0.4. Therefore, when the meteorological conditions can be retrieved relatively
316 accurately, particulate matter assimilation is the key to improving the simulative skill of
317 pollutants.

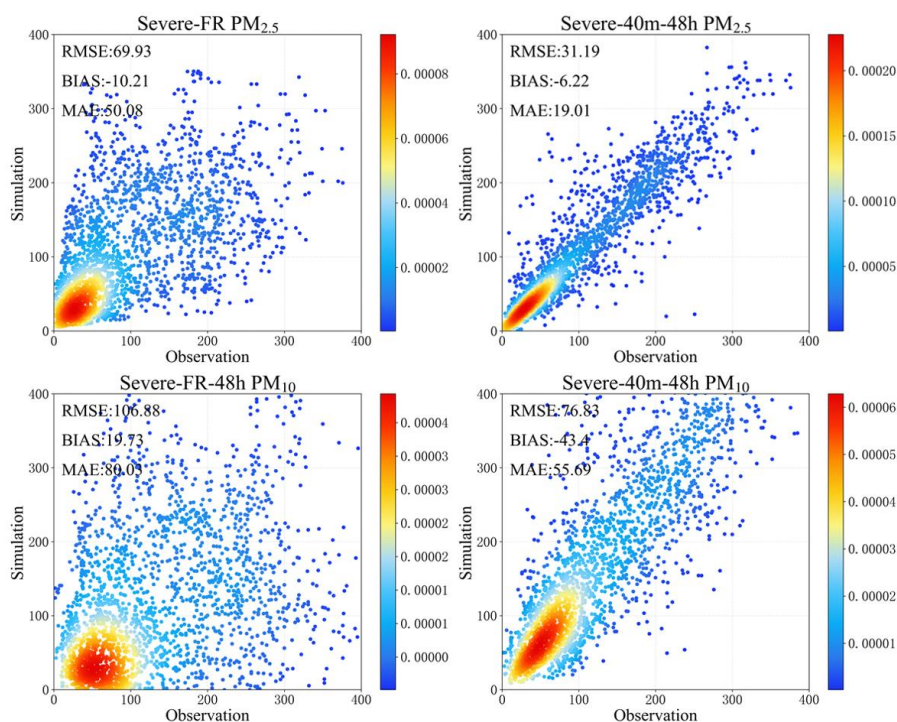


318
319 Figure3. (a) Temporal variation about air quality index at six sites in severe haze event. (b) A
320 Taylor graph describing simulation from Severe-FR about five kinds of parameters compared
321 with the observed ones in BTH region.

322 3.1.2 The improvement of the severe haze simulation achieved by 4D-LETKF



323 The divergence between assimilation and control experiment reflects the contribution from
324 4D-LETKF adjustment. Consequently, the study takes an ensemble member size of 40 and
325 assimilation window length of 48 hours to conduct sensitivity experiment and compare with
326 Severe-FR-48h which has the same integration time in each cycle to validate the effectiveness
327 of 4D-LETKF assimilation system (the analysis from the selection of 40 ensemble members
328 and 48 hours of assimilation window length is presented here because it shows the best
329 performance among sensitivity experiments in the next section). Figure 4 reveals the
330 performance of control and assimilation experiments in severe haze event. The RMSE values
331 of $PM_{2.5}$ and PM_{10} in Severe-FR-48h are 69.93 and $106.88\mu\text{g m}^{-3}$ and both with scattered
332 distribution, indicating substantial uncertainty exist in reproducing this severe haze event. In
333 Severe-40m-48h, the RMSE values of $PM_{2.5}$ and PM_{10} are 31.19 and $76.83\mu\text{g m}^{-3}$, decreasing
334 by 55.40% and 28.12% respectively in a high particulate matter concentration environment.
335 The decreased RMSE values also imply that the assimilation system has reached a well-
336 calibrated stage. Not only more points are getting together, but smaller simulation errors for
337 $PM_{2.5}$ and PM_{10} also imply that the Severe-40m-48h outperforms the Severe-FR-48h in this
338 severe haze event.



339

340 Figure 4. Scatter and density plot of PM_{2.5} and PM₁₀ in Severe-FR-48h and Severe-40m-

341 48h versus observations from verification stations (units: $\mu\text{g m}^{-3}$).

342 In order to acquire basis distribution of simulation errors for particulate matter, Figure 5

343 presents the frequency distribution of deviations between observed and simulated particulate

344 matter concentrations in Sevre-FR-48 and Severe-40m-48h experiments. It is obviously that

345 Severe-40m-48h increases the frequency of low deviations and decrease those of high

346 deviations in the simulation of PM_{2.5}. The deviation pattern of PM_{2.5} in Severe-40m-48h is

347 generally squeezed with higher peaking and symmetrical to the value of 0 than Severe-FR-48h.

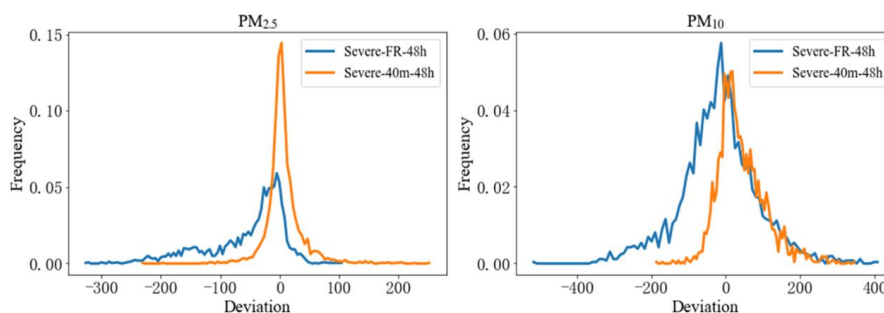
348 For the deviation distribution pattern of PM₁₀, it shows high frequency of negative deviations

349 and great underestimation in the Severe-FR-48h, and this underestimation has been effectively

350 corrected by the adjustment of initial conditions and step analysis in Severe-40m-48h. Specially,



351 the proportion of deviation within $20 \mu\text{g m}^{-3}$ in the Severe-40m-48h is 69.98% for $\text{PM}_{2.5}$ and
352 31.90% for PM_{10} .

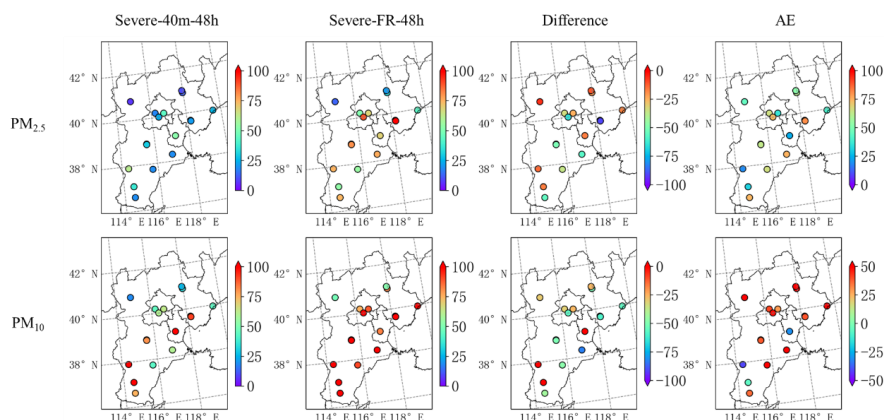


353

354 Figure 5. Frequency distribution of the deviations about the simulated $\text{PM}_{2.5}$ and PM_{10}

355 concentrations in Severe-40m-48h and Severe-FR-48h minus the observed ones.

356 Figure 6 exhibits the spatial distribution of four statistical parameters about RMSE for
357 particulate matter among the BTH region. By comparison from the Severe-FR-48h and Severe-
358 40m-48h, there are significant RMSE reduction for $\text{PM}_{2.5}$ after assimilation, implying that the
359 actual evolution of $\text{PM}_{2.5}$ can be better represented by Severe-40m-48h. For instance, the RMSE
360 values of $\text{PM}_{2.5}$ in Baoding, Hengshui and Cangzhou, have significantly decreased to 29.85,
361 18.98, and $19.06 \mu\text{g m}^{-3}$, respectively, compared to 80.55, 55.22 and $76.32 \mu\text{g m}^{-3}$ in the Severe-
362 FR-48h. AE in most verification stations has exceeded 50% also suggests the high efficiency
363 of 4D-LETKF assimilation for the simulation of $\text{PM}_{2.5}$. Although the performance of
364 assimilation experiment in Shijiazhuang city does not have a good agreement with observation
365 and shows a positive difference, high values of AE in most of verification stations also proves
366 the validation of assimilating effect for PM_{10} . Compared to the Severe-FR-48h, the Severe-
367 40m-48h productively reduces the RMSE of PM_{10} , accompany with high values of 61.18%,
368 59.17% and 52.18% about AE on Zhangjiakou, Tangshan and Hengshui, respectively.



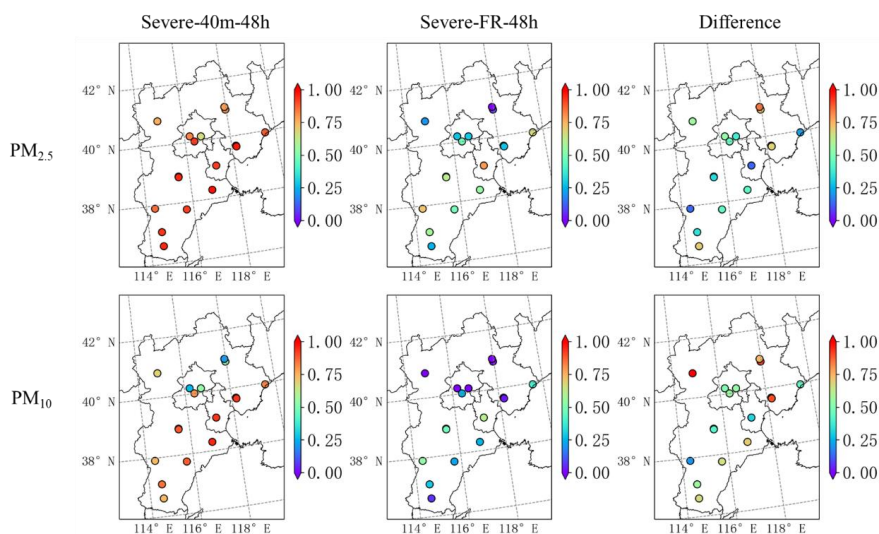
369

370 Figure 6. Spatial distribution of RMSE values from Severe-40m-48h (first column), Severe-
371 FR-48h (second column), their difference (third column) and AE (fourth column) for $PM_{2.5}$
372 (first row) and PM_{10} (second row) from 15 January to 21 January among verification station
373 in BTH region. The difference implies the RMSE in Severe-40m-48h minus those in Severe-
374 FR-48h. AE is assimilation efficiency and has been described in methodology before.

375 The spatial distribution of correlation coefficients from Severe-40m-48h, Severe-FR-48h,
376 their difference for $PM_{2.5}$ and PM_{10} are also illustrated in Figure 7. The assimilation experiment
377 increases the correlation coefficients to more than 0.6 at all sites in the simulations of $PM_{2.5}$ and
378 exceed 0.7 among the southern BTH region in the simulations of PM_{10} . The Severe-40m-48h
379 also reverses the opposite trend of $PM_{2.5}$ and PM_{10} series in Severe-FR-48h versus observations,
380 for example, the correlation coefficients in Severe-FR-48h at Chengde and Zhangjiakou are -
381 0.42 and -0.53, but increase to 0.52 and 0.69 after assimilation in the simulations of PM_{10} .
382 Incorporating more assimilable observations may further increase the correlation coefficient in
383 the simulation of particulate matter (Kong et al., 2021). Data assimilation by multiple
384 observations from diverse platform is necessary because it can integrate and coordinate
385 observational information into aerosol forecasts well and then improve air pollutant forecast



386 accuracy (Barbu et al., 2009, Ma et al., 2020).



387

388 Figure 7. Spatial distribution of correlation coefficients from Severe-40m-48h (first column),

389 Severe-FR-48h (second column), their difference (third column) for $PM_{2.5}$ (first row) and

390 PM_{10} (second row) from 15 January to 21 January among verification station in BTH region.

391 The difference implies the correlation coefficient in Severe-40m-48h minus those in Severe-

392 FR-48h.

393 The temporal variations of particulate matter from Severe-40m-48h, Severe-FR-48h and

394 observation at six independent verification stations are shown in Figure S1 and Figure S2. The

395 six independent verification stations have experienced different levels of air pollution and

396 distributed uniformly over BTH region. It is apparently that the analysis at six stations have

397 good agreement with observations both for $PM_{2.5}$ and PM_{10} , which can better characterize the

398 peaks and valleys of particulate matter concentration over investigated period.

399 Table 3 lists the Δ RMSE, Δ CORR and AE in the simulations of particulate matter at

400 independent stations outside the BTH region. The RMSEs and correlation coefficients have



401 decreased and increased respectively after assimilate ground-based observations, suggesting
402 that the uncertainty in Severe-FR-48h has been well optimized not only in the BTH region, but
403 also includes the whole simulation domain. Compared to the Severe-FR-48h, the analysis in
404 Yuncheng shows that the RMSE values of $PM_{2.5}$ and PM_{10} have decreased by 98.26 and 144.56
405 $\mu g m^{-3}$ remarkably, such a great improvement may relate to the enhanced estimation capability
406 about state variables of particulate matter. The high values of AE also suggest that verification
407 observation sites outside the BTH region have achieved a good Kalman gain. In previous
408 researches, predicting heavy haze events in northern China, especially over the Beijing-Tianjin-
409 Hebei Region, remained a challenge when compared to other regions like Pearl River Delta and
410 Yangtze River Delta in China (Feng et al., 2018, Gao et al., 2017). The deficiency may be
411 induced by GFS (National Centers for Environmental Prediction Global Forecast System) data,
412 providing a poor estimation of meteorological fields in northern China, increasing the
413 instability of atmospheric dynamics and ultimately decreasing the assimilation effect (Kong et
414 al., 2021). In this research, the analysis is propagated by meteorological elements including
415 temperature, air pressure and wind fields come from NCEP Final analysis data, which may
416 provide an optimal meteorological boundary conditions for the assimilation of pollutant
417 concentration.

418 Table 3. Statistics about $PM_{2.5}$ and PM_{10} from analysis in the cities among neighboring
419 provinces of BTH region. Δ RMSE (Δ CORR) represent the RMSE (correlation coefficient)
420 from analysis minus those from Severe-FR-48h.

City/ Statistical	$PM_{2.5}$			PM_{10}		
	Δ RMSE	Δ CORR	AE	Δ RMSE	Δ CORR	AE



variable						
Taiyuan	-21.30	+0.41	23.93%	-54.8	+0.71	39.05%
Changzhi	-38.39	+0.38	65.93%	-63.06	+0.68	63.22%
Jincheng	-37.94	+0.37	66.85%	-94.32	+0.89	72.45%
Shuozhou	-27.07	+0.31	58.96%	-100.08	+0.84	69.96%
Yuncheng	-98.26	+0.67	77.85%	-144.56	+1.25	80.64%
Hohhot	-92.30	+0.67	74.53%	-121.79	+1.41	68.92%
Chifeng	-16.90	+0.55	64.95%	-38.18	+0.95	60.85%
Huludao	-38.56	+0.20	59.11%	-95.95	+1.04	65.76%
Jinzhou	-42.97	+0.21	61.17%	-46.26	+0.83	45.83%
Chaoyang	-39.37	+0.37	51.14%	-83.04	+1.23	61.86%
Jinan	-44.90	+0.63	69.71%	-71.22	+0.59	62.93%
Qingdao	-23.99	+0.27	37.98%	-72.05	+0.44	72.21%
Shouguang	-28.70	+0.21	58.03%	-48.92	+0.39	47.57%
Anyang	-35.87	+0.41	62.53%	-32.08	+0.60	33.15%
Zhengzhou	-26.26	+0.37	37.51%	-3.64	+0.42	3.73%

421 3.2 The sensitivity of 4D-LETKF to ensemble member size and length of assimilation

422 window

423 In previous section, the research has compared the performance from assimilation

424 experiment with 40 ensemble members and 48 hours of assimilation window length against that

425 do not integrate hourly pollutant observations. The results fully demonstrate the ability of 4D-

426 LETKF assimilation method to reproduce severe haze events in spatial and temporal dimension.

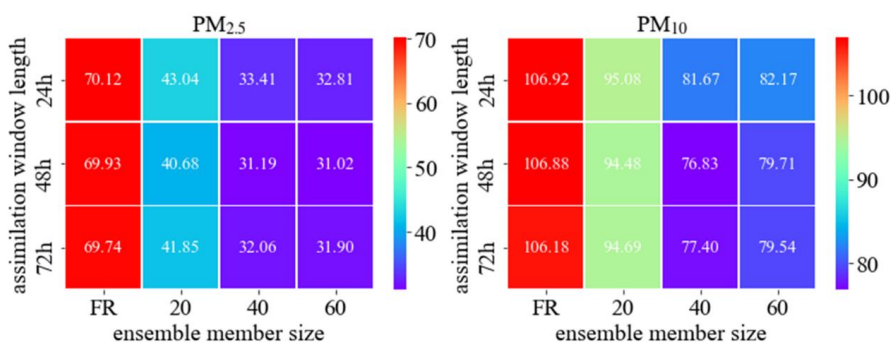


427 However, the 4D-LETKF assimilation effect is highly rely on selection of ensemble member
428 size and length of assimilation window, so how does the assimilation approach vary to the
429 parameterized selection in severe haze event? It is of great meaning to conduct sensitivity
430 experiments based on ensemble member size and length of assimilation window, compare each
431 performance of them by statistical metrics, and summarize the general influence rule of 4D-
432 LETKF parameter selection. Consequently, nine panels of sensitivity experiments are
433 conducted with the selection of ensemble member size (20, 40, 60 members) and the length of
434 assimilation window (24, 48, 72 hours) to maximize the positive innovation in this section.

435 Figure 8 reveals the heatmap about RMSE in each sensitivity experiment of particulate
436 matter over verification sites among the BTH region. The results of free run experiment with
437 different integration times (24, 48, 72 hours) are offered here for comparison with analysis
438 which with same assimilation cycle time. The RMSEs of $PM_{2.5}$ and PM_{10} in each free run
439 experiment exceed $60\mu g m^{-3}$ and $100\mu g m^{-3}$, respectively. It is apparently that the 4D-LETKF
440 performs better than the FR experiment in the simulation about $PM_{2.5}$ and PM_{10} over wide range
441 of ensemble member sizes and assimilation window lengths, illustrating the broad applicability
442 of 4D-LETKF data assimilation to these parameters. However, it can be found that the analysis
443 of $PM_{2.5}$ and PM_{10} are dependent on length of assimilation window and dramatically related to
444 ensemble member size in all sensitivity experiments. Unlike the short-lived and chemical
445 reactive species (such as SO_2 and NO_2) which easily undergo complex and nonlinear
446 photochemical reactions, a relative longer assimilation window length seems more suitable for
447 assimilating ground-based particulate matter observations (Peng et al., 2017, Kong et al., 2021).
448 A longer assimilation window length could also avoid the underestimation of model spread and



449 overconfidence in the first-guess state estimate by enough integration time of each member
450 (Schutgens et al., 2010, Miyazaki et al., 2012a, Hunt et al., 2007). Hence, 48 or 72 hours of
451 assimilation window length are advised to optimize the ensemble concentration trajectories. On
452 the other hands, increasing ensemble member size efficiently reduces uncertainty in $PM_{2.5}$ and
453 PM_{10} , as evidenced by the decrease of RMSEs from free run to assimilation experiments with
454 20 and 40 members. However, when compared with the results from 40 ensemble members,
455 the accuracy of numerical simulations has not significantly improved for both $PM_{2.5}$ and PM_{10}
456 with 60 ensemble members, indicating that 40 members are sufficient and feasible to provide a
457 reliable estimation of the background error and analysis rather than more numerical source
458 consumption. Considering numerical source consumption and RMSE values in the simulations
459 of $PM_{2.5}$ and PM_{10} , the Severe-40m-48h shows more comparable to the observations when
460 compared with the other eight panels of sensitivity experiments.



461
462 Figure 8. Heatmap about RMSE in each sensitivity experiment of particulate matter over
463 verification sites (units: $\mu\text{g m}^{-3}$). The number in each small square represents the RMSE
464 between observation and simulation for each combination of ensemble member size and the
465 length of assimilation window methods.

466 3.3 The influence from ensemble member size to the ensemble spread



467 In order to explore why increasing ensemble member size can efficiently reduce the
468 uncertainty in the analysis of $PM_{2.5}$ and PM_{10} as revealed in Figure 8, the study investigates the
469 spatial distribution of standard deviations of $PM_{2.5}$ and $PM_{10-2.5}$ among first guess and analysis
470 field in terms of ensemble members. The standard deviations of ensemble members describe
471 how the emission perturbation propagates among the forward model, and this perturbation is
472 driven by the underlying surface pollution emission inputs and the meteorological conditions.
473 Therefore, the standard deviation in the first guess fields quantifies the dispersion degree of the
474 ensemble background, substantially impacts the calculation of assimilation parameters such as
475 ensemble state vector perturbations, and further affects the performance of particulate matter
476 predictions.

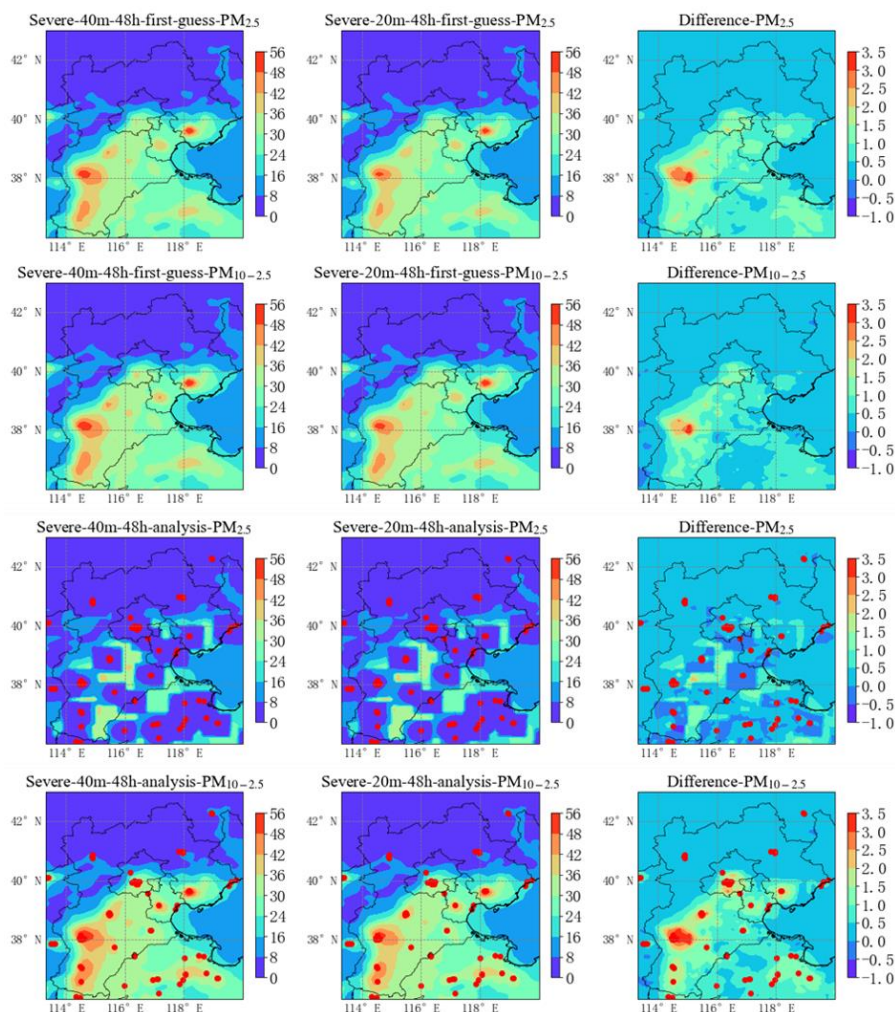
477 Since the RMSE decreases with the increasing ensemble member size when 20 and 40
478 members are setting, and 48 hours of assimilation window length corresponds to a smaller
479 RMSE, the study compares the spatial distribution of ensemble standard deviations from
480 Severe-20m-48h and Severe-40m-48h to explain the relationship between ensemble member
481 size and simulation errors in analysis result. Figure 9 depicts contour maps of the spatial
482 distribution of temporal averaged standard deviations in the first guess and analysis of Severe-
483 40m-48h, Severe-20m-48h and their difference for $PM_{2.5}$ and $PM_{10-2.5}$ during severe haze event.
484 The first guess in Severe-40m-48h and Severe-20m-48h shows that the relatively high standard
485 deviations are generally observed in southern of BTH region, while those in the northern areas
486 are close to zero for both $PM_{2.5}$ and $PM_{10-2.5}$. High value centers are distributed in densely
487 populated areas and urban centers including Shijiazhuang, Xingtai, Tianjin and Tangshan city,
488 where the standard deviations have generally exceeded $30\mu g m^{-3}$. Combined with Figure S3, it



489 can be seen that the areas with large concentration standard deviations correspond well with the
490 spatial distribution of anthropogenic emission and the areas with large standard deviations of
491 emission sources. The standard deviations of concentrations of $PM_{2.5}$ and $PM_{10-2.5}$ have closely
492 relationship with the allocation and configuration of anthropogenic emission sources, because
493 disturbances are only added to emission sources for each ensemble member, without disturbing
494 the meteorological field in this haze event. The variation of difference in the third column
495 entirely comes from increasing ensemble member size. The positive difference between Severe-
496 40m-48h and Severe-20m-48h in first guess suggests that increasing ensemble member size
497 leads to greater differences among each ensemble for both $PM_{2.5}$ and $PM_{10-2.5}$ over BTH areas.
498 The high efficiency of 4D-LETKF is strongly influenced by sufficient information spread
499 among ensemble members, which integrate spreading observational information to produce
500 analysis from the first guess (Rubin et al., 2016). As a result, the increasing ensemble member
501 size improves divergence for each member and facilitates the state vectors about $PM_{2.5}$ and
502 $PM_{10-2.5}$ information spread in the first guess, which makes a better performance for Severe-
503 40m-48h rather than Severe-20m-48h in this severe haze event. The standard deviations of
504 $PM_{2.5}$ in analysis are generally lower than those in first guess. Due to the localization of 4D-
505 LETKF, that is the ground-based observation data only optimized for simulation grid within a
506 certain range, square-like areas of low standard deviations appear in the analysis of $PM_{2.5}$ both
507 for 40 and 20 ensemble members. Nearly all assimilated stations are located at the center of
508 low value square areas suggesting that 4D-LETKF tunes all $PM_{2.5}$ trajectories into a small range
509 with low standard deviation at each slot of analysis by the assimilation of ground-based
510 observations. For $PM_{10-2.5}$, there are no square-like areas of low standard deviations in the



511 analysis both for 40 and 20 ensemble members, indicating that the 4D-LETKF does not has an
512 obvious limitation for $PM_{10-2.5}$ trajectories, however, the decreased standard deviations effect
513 from the 4D-LETKF is still distinct for the particulate matter because PM_{10} consist of $PM_{2.5}$
514 and $PM_{10-2.5}$ in simulation. Enlarging ensemble member size is benefit to the improving of
515 standard deviations of $PM_{2.5}$ and $PM_{10-2.5}$ in analysis, while the improving magnitude of $PM_{2.5}$
516 is obviously smaller than $PM_{10-2.5}$. The assimilation results are not directly influenced by the
517 increased standard deviations in analysis. Such low increasement of standard deviations
518 (generally below $3 \mu\text{g m}^{-3}$) is unlikely to induce uncertainty in the fitting and averaging process,
519 but facilitates divergence in initial conditions between forecasting members in the next
520 assimilation cycle. In addition, Figure S4 depict the spatial distribution of standard deviation
521 from Severe-60m-48h, Severe-20m-48h and their difference in the first guess and analysis field.
522 It can be seen that increasing the number of ensemble member generally also improves the
523 standard deviation in first guess and analysis over the BTH region both for $PM_{2.5}$ and $PM_{10-2.5}$.
524 Overall, the increasement of standard deviations generated by increasing ensemble member
525 size directly improves the information spread of ensemble members in the first guess field and
526 the assimilation effect of 4D-LETKF, while the positive difference of standard deviation in
527 analysis favors the variances between each initial condition in the next assimilation window
528 during severe haze event.



529

530 Figure 9. Contour maps of spatial distributions of temporal averaged $PM_{2.5}$ and $PM_{10-2.5}$
531 standard deviations in the first guess (first and second row) and analysis (third and fourth
532 row) of Severe-40m-48h, Severe-20m-48h and their difference (Severe-40m-48h minus
533 Severe-20m-48h) within simulation period (units: $\mu\text{g m}^{-3}$). The red dots in analysis of $PM_{2.5}$
534 and $PM_{10-2.5}$ implies the location of assimilated stations.

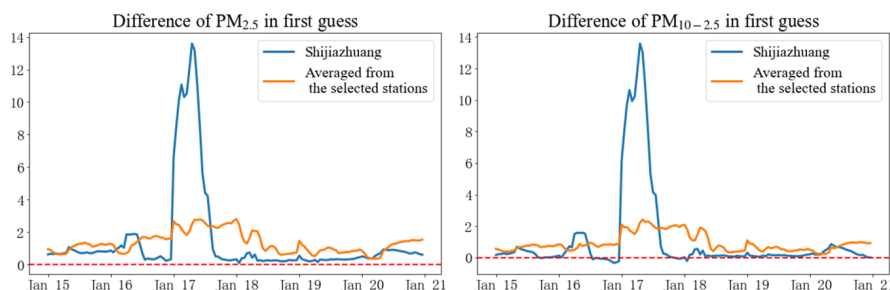
535 In the other sides, no matter for the first guess from Severe-40m-48h or Severe-20m-48h,
536 the high standard deviations are found near Shijiazhuang region in Figure 9, but Shijiazhuang



537 station still with larger RMSE and smaller AE in Figure 6. This seems contrary to the opinion
538 that increasing standard deviations in the first-guess field is beneficial to raising the accuracy
539 of pollutant simulations. Therefore, Shijiazhuang station and the stations which with high
540 values of AE (exceed 50) and difference of standard deviation in first guess (exceed $1 \mu\text{g m}^{-3}$)
541 including Beijing, Tangshan, Handan, Baoding, Cangzhou, and Hengshui regions are selected
542 to explore the temporal distribution of standard deviations difference between 40 and 20
543 ensemble members, so as to further advance our understanding about the relationship between
544 ensemble member size and simulation uncertainty in 4D-LETKF system. Figure 10 examines
545 the temporal distribution of the standard deviation difference for $\text{PM}_{2.5}$ and $\text{PM}_{10-2.5}$ during the
546 investigated period at Shijiazhuang station and results averaged from the selected stations.
547 From January 17 to January 18, the standard deviation difference in first guess at Shijiazhuang
548 station has increased drastically and exceeded up to $10 \mu\text{g m}^{-3}$ for both $\text{PM}_{2.5}$ and $\text{PM}_{10-2.5}$. This
549 uneven temporal distribution results in a large standard deviation difference of first guess in
550 Figure 9. This huge divergency between ensemble member may attributed to the peak pollutant
551 levels with AQI exceeds 300 at Shijiazhuang station occurs on the January 17 as shown in
552 Figure 3. In highly polluted environments, 40 forecasting members with different perturbations
553 in emission sources are more likely to differ the concentration of particulate matter in first guess
554 fields. Excessive high dispersion of $\text{PM}_{2.5}$ and $\text{PM}_{10-2.5}$ for ensemble members may arise an
555 over-high estimation about background covariances and obtain a poor Kalman gain. Moreover,
556 it can be found that the standard deviation difference of $\text{PM}_{2.5}$ and $\text{PM}_{10-2.5}$ at Shijiazhuang
557 station are obviously lower than the averaged from selected stations except the high dispersion
558 time, suggesting the increasing number of ensemble members has limited impact on the



559 divergence between each ensemble member at Shijiazhuang during these dates. Too low
560 standard deviations imply filter convergence near Shijiazhuang station, which may induce the
561 underestimation of model spread, reduce the effect of observation information, and make
562 system more certain of state estimate about particulate matter concentrations in first guess
563 (Hunt et al., 2007). In addition, reducing uncertainty in the mixed anthropogenic emission
564 inventory may be an important approach to avoid filter convergence near the Shijiazhuang
565 region. Generally edited by empirical and statistical data such as anthropogenic emission
566 factors and activity dataset, the anthropogenic emissions based on bottom-up method can hardly
567 capture the real spatiotemporal distribution of anthropogenic emissions over China as
568 frequently variations in energy consumption, even though the latest version. Among the
569 southern of BTH region, the great positive innovations of particulate matter emissions in
570 posterior estimation have been discovered in previous researches, implying that the update of
571 underestimated emissions in this region may enlarge the deviations between ensemble members
572 since a large quantity of emissions corresponds to a higher degree of perturbation (Peng et al.,
573 2017, Feng et al., 2023). In a word, the perturbations added to emissions and meteorological
574 fields needs to be executed carefully in 4D-LETKF system to avoid too high or too low
575 ensemble dispersion degree because which determinate how analysis results weight toward
576 observations information and first guess fields (Dai et al., 2021).



577

578 Figure 10. Temporal distribution of standard deviation difference (Severe-40m-48h minus
579 Severe-20m-48h) in first guess for $PM_{2.5}$ and $PM_{10-2.5}$ at Shijiazhuang station and averaged
580 from the selected stations (units: $\mu g m^{-3}$). The red dash line is zero.

581 The results above suggest that the increasing ensemble member size strengthens divergence,
582 benefits the information spread in the first guess and finally improves the simulative skill in
583 severe haze event. However, it has not been testified whether these influence rules are also
584 practical for a more common, and less polluted condition. Therefore, two assimilation
585 experiments in moderate haze event, Moderate-20m-48h and Moderate-40m-48h, are
586 performed to examine the applicable range. As shown in Figure S5, the moderate haze event
587 spans from 00:00 UTC 15 January 2019 to 00:00 UTC 21. This moderate event began on 15
588 January, with AQI increasing until 18 January, reaching a moderate level but not lasting for a
589 long time, and then decreased on 19 and 20 January. Most areas experienced mild or moderate
590 air pollution, with AQI generally below 200, the primary pollutant was particulate matter after
591 calculation. The simulations of moderate haze event utilize the same anthropogenic emission
592 inventory as used in severe haze event since two events both happen in January, thereby avoids
593 the additional influence introduce from emission source variation and the perturbations to
594 information spread and assimilation effect.

595 Figure S6 shows the simulated concentrations of $PM_{2.5}$ and PM_{10} against ground-based



596 observations during moderate air pollution event. The RMSEs of $PM_{2.5}$ in Moderate-FR-48h,
597 Moderate-20m-48h and Moderate-40m-48h are 40.40, 24.12 and $18.52\mu\text{g m}^{-3}$, respectively, and
598 the RMSEs of PM_{10} are 73.47, 67.81 and $57.04\mu\text{g m}^{-3}$ respectively. The concentrations of $PM_{2.5}$
599 and PM_{10} in assimilation experiments are more in agreement with observations, suggesting the
600 validation of 4D-LETKF adjustment in moderate haze event. The phenomena that the
601 simulation error of $PM_{2.5}$ and PM_{10} decrease with increasing ensemble member size are same
602 with those characteristics have shown in severe haze event before.

603 Similar to Figure 9, Figure S7 presents the spatial distributions of standard deviations about
604 $PM_{2.5}$ and PM_{10} in the first guess of Moderate-40m-48h, Moderate-20m-48h and their
605 difference. The relatively smaller magnitude of standard deviation difference in first guess may
606 relate to relatively low $PM_{2.5}$ and PM_{10} concentrations in moderate haze event. Positive
607 difference in first guess and analysis for particulate matter implies the Moderate-40m-48h
608 obtains a higher diversity of ensemble members than Moderate-20m-48h, and which are also
609 similar with those happen in the severe haze event.

610 4. Summary

611 The numerical simulation of severe haze events with air quality index larger than 200 has
612 been a challenging problem in the field of atmospheric pollution for a long time. In this research,
613 a WRF-Chem/4D-LETKF coupled data assimilation system has been successfully developed
614 by ensemble member with perturbed anthropogenic emissions to improve the simulative skill
615 of particulate matter in severe haze event during the winter of 2020. The research validated the
616 effectiveness of 4D-LETKF data assimilation, discussed the optimal parameter combination of
617 ensemble member size and length of assimilation window for 4D-LETKF assimilation system,



618 summarized and explained the influence rules from parametric selection to the 4D-LETKF
619 assimilation effect during severe and moderate haze event.

620 It is concluded that the Severe-40m-48h experiment shows the best performance in the
621 simulations of $PM_{2.5}$ and PM_{10} after comparing the statistical errors and computing resource
622 consumption across multiple sensitivity analyses, with the RMSEs of 31.19 and $76.83 \mu\text{g m}^{-3}$
623 for $PM_{2.5}$ and PM_{10} in severe haze event. Severe-40m-48h optimizes the underestimation of
624 particulate matter concentrations in Severe-FR-48h, and remarkably improves the simulation
625 accuracy in the entire BTH region and neighboring provinces. For example, the RMSEs of
626 $PM_{2.5}$ in Baoding, Hengshui and Cangzhou decrease to 29.85, 18.98 and $19.06 \mu\text{g m}^{-3}$
627 respectively, from 80.55, 55.22 and $76.32 \mu\text{g m}^{-3}$ in Severe-FR-48h. Severe-40m-48h is also
628 capable of retrieving the peaks and valleys of particulate matter concentration over investigated
629 period. To examine the dependence of the assimilation effect of 4D-LETKF, nine panels of
630 sensitivity tests were conducted according to ensemble member size and length of assimilation
631 window. The findings suggest that the simulation accuracy of $PM_{2.5}$ and PM_{10} can be strongly
632 improved by the increasing ensemble member size from 20 to 40. A relative longer assimilation
633 window length such as 48 or 72 hours combine with 40 ensemble member size is advised in
634 4D-LETKF assimilation system. In view of performance of ensemble member, increasing
635 ensemble member size improves divergence among each forecasting member, facilitates the
636 spread of state vectors about $PM_{2.5}$ and PM_{10} information in the first guess, favors the variances
637 between each initial condition in the next assimilation window and leads to better performance
638 in simulation of severe haze event. A similar conclusion can also be draw from the moderate
639 haze event, suggesting that this influence rule is applicable in both severe and moderate haze



640 conditions.

641 There are still some deficiencies in this research. Although we have performed data quality
642 control in this study, we did not use approaches such as super-observations to improving the
643 correspondence between grid points and observations (Jin et al., 2022, Miyazaki et al., 2012a),
644 which may increase the representational error and result in the possibility of two stations with
645 different concentrations interpolating in the same grid. Improving the spatial resolution of
646 forward model or introducing super observations may mitigate this problem (Miyazaki et al.,
647 2012b, Feng et al., 2020b). Furthermore, the concentration of state variables about particulate
648 matters in initial conditions are optimized in this study, but there still remain large uncertainties
649 in anthropogenic emission data, which is an important chemical boundary input for pollutant
650 simulations. These uncertainties sources may play a significant role in the over- or
651 underestimation of pollutant ensemble modeling. The anthropogenic emissions inversion based
652 on Ensemble Kalman filter and their variants is recognized as an effective approach for
653 reducing uncertainty in anthropogenic emission sources (Peng et al., 2018, Feng et al., 2020a,
654 Chen et al., 2019b). The jointly adjust initial conditions and emissions source with 4D-LETKF
655 is the focus of future work to further improving the forecast skills about air pollutants during
656 heavy pollution events.

657

658 CRediT authorship contribution statement

659 **Jianyu Lin**: Conceptualization, Formal analysis, Visualization. **Tie Dai**: Investigation,
660 Methodology, Resources, Supervision. **LiFang Sheng**: Funding acquisition, Project
661 administration. **Weihang Zhang**: Writing - original draft, Data curation. **Shangfei Hai**: Writing



662 - review and editing. **Yawen Kong**: Validation.

663

664 Declaration of competing interest

665 The authors declare that they have no conflict of interest.

666 Acknowledgements

667

668 Financial support. This work is supported by the National Natural Science Foundation of China

669 (No. 42275191), National Natural Science Funds of China (42375190).

670

671 Code and data availability

672 The code and data in this research are available in <https://zenodo.org/records/14010521>, and

673 we are grateful to the relevant researchers who make contributions to WRF-Chem model and

674 LETKF method (Miyoshi, 2024).

675

676 Reference

677

678 Anderson, J. L.: An adaptive covariance inflation error correction algorithm for ensemble filters,

679 Tellus, 59A, 210–224, <https://doi.org/10.1111/j.1600-0870.2006.00216.x>, 2007.

680

681 Barbu, A. L., Segers, A. J., Schaap, M., Heemink, A. W., and Buitjes, P. J. H.: A multi-

682 component data assimilation experiment directed to sulphur dioxide and sulphate over Europe,

683 Atmospheric Environment, 43(9), 1622–1631, <https://doi.org/10.1016/j.atmosenv.2008.12.005>,



684 2009.

685

686 Benedetti, A., Morcrette, J., Boucher, O., Dethof, A., Engelen, R. J., Fisher, M., Flentje, H.,
687 Huneeus, N., Jones, L., Kaiser, J. W., Kinne, S., Mangold, A., Razinger, M., Simmons, A. J.,
688 and Suttie, M.: Aerosol analysis and forecast in the European Centre for Medium-Range
689 Weather Forecasts Integrated Forecast System: 2. Data assimilation, *J. Geophys. Res.*, 114,
690 D13205, <https://doi.org/10.1029/2008JD011115>, 2009.

691

692 Cheng, Y., Dai, T., Goto, D., Schutgens, N. A. J., Shi, G., and Nakajima, T.: Investigating the
693 assimilation of CALIPSO global aerosol vertical observations using a four-dimensional
694 ensemble Kalman filter, *Atmos. Chem. Phys.*, 19, 13445–13467, [https://doi.org/10.5194/acp-](https://doi.org/10.5194/acp-19-13445-2019)
695 [19-13445-2019](https://doi.org/10.5194/acp-19-13445-2019), 2019.

696

697 Chen, D., Liu, Z., Ban, J., and Chen, M.: The 2015 and 2016 wintertime air pollution in China:
698 SO₂ emission changes derived from a WRF-Chem/EnKF coupled data assimilation system,
699 *Atmos. Chem. Phys.*, 19, 8619–8650, <https://doi.org/10.5194/acp-19-8619-2019>, 2019a.

700

701 Chen, D., Liu, Z., Ban, J., Zhao, P., and Chen, M.: Retrospective analysis of 2015–2017
702 wintertime PM_{2.5} in China: response to emission regulations and the role of meteorology, *Atmos.*
703 *Chem. Phys.*, 19, 7409–7427, <https://doi.org/10.5194/acp-19-7409-2019>, 2019b.

704

705 Dai, T., Cheng, Y., Goto, D., Li, Y., Tang, X., Shi, G., and Nakajima, T.: Revealing the sulfur



706 dioxide emission reductions in China by assimilating surface observations in WRF-Chem,
707 Atmos. Chem. Phys., 21, 4357–4379, <https://doi.org/10.5194/acp-21-4357-2021>, 2021.

708

709 Dai, T., Cheng, Y., Suzuki, K., Goto, D., Kikuchi, M., Schutgens, N. A. J., Yoshida, M., Zhang,
710 P., Husi, L., Shi, G., and Nakajima, T.: Hourly Aerosol Assimilation of Himawari-8 AOT Using
711 the Four-Dimensional Local Ensemble Transform Kalman Filter, J. Adv. Model. Earth Syst.,
712 11, 680–711, <https://doi.org/10.1029/2018MS001475>, 2019.

713

714 Elbern, H., Strunk, A., Schmidt, H., and Talagrand, O.: Emission rate and chemical state
715 estimation by 4-dimensional variational inversion, Atmospheric Chemistry and Physics, 7(14),
716 3749–3769, <https://doi.org/10.5194/acp-7-3749-2007>, 2007.

717

718 Evensen, G.: Sequential data assimilation with a nonlinear quasi-geostrophic model using
719 Monte Carlo methods to forecast error statistics, Journal of Geophysical Research: Oceans, 99,
720 10143–10162, <https://doi.org/10.1029/94JC00572>, 1994.

721

722 Evensen, G.: The Ensemble Kalman Filter: theoretical formulation and practical
723 implementation, Ocean Dynam, 53, 343–367, <https://doi.org/10.1007/s10236-003-0036-9>,
724 2003.

725

726 Feng, S., Jiang, F., Jiang, Z., Wang, H., Cai, Z., and Zhang, L.: Impact of 3DVAR assimilation
727 of surface PM_{2.5} observations on PM_{2.5} forecasts over China during wintertime, Atmospheric



728 Environment, 187, 34-49, <https://doi.org/10.1016/j.atmosenv.2018.05.049>, 2018.

729

730 Feng, S., Jiang, F., Wang, H., Wang, H., Ju, W., Shen, Y., Zheng, Y., Wu, Z., and Ding,

731 A.: NO_x emission changes over China during the COVID-19 epidemic inferred from surface

732 NO₂ observations, Geophysical Research Letters, 47, e2020GL090080,

733 <https://doi.org/10.1029/2020GL090080>, 2020a.

734

735 Feng, S., Jiang, F., Wu, Z., Wang, H., Ju, W., and Wang, H.: CO emissions inferred from surface

736 CO observations over China in December 2013 and 2017, Journal of Geophysical Research:

737 Atmospheres, 125, <https://doi.org/10.1029/2019JD031808>, 2020b.

738

739 Feng, S., Jiang, F., Wu, Z., Wang, H., He, W., Shen, Y., Zhang, L., Zheng, Y., Lou, C., Jiang, Z.,

740 and Ju, W.: A Regional multi-Air Pollutant Assimilation System (RAPAS v1.0) for emission

741 estimates: system development and application, Geosci. Model Dev., 16, 5949–5977,

742 <https://doi.org/10.5194/gmd-16-5949-2023>, 2023.

743

744 Gao, M., Saide, P. E., Xin, J., Wang, Y., Liu, Z., Wang, Y., Wang, Z., Pagowski, M., Guttikunda,

745 S. K., and Carmichael, G. R.: Estimates of Health Impacts and Radiative Forcing in Winter

746 Haze in Eastern China through Constraints of Surface PM_{2.5} Predictions, Environmental

747 Science & Technology, 51(4), 2178-2185, <https://doi.org/10.1021/acs.est.6b03745>, 2017.

748



749 Grell, G. A.: Prognostic Evaluation of Assumptions Used by Cumulus Parameterizations, Mon.
750 Wea. Rev., 121, 764–787, <https://doi.org/10.1175/1520->
751 0493(1993)121<0764:PEOAUB>2.0.CO;2, 1993.

752

753 Grell, G., Peckham, S. E., Schmitz, R., McKeen, S. A., Frost, G., Skamarock, W. C., and Eder,
754 B.: Fully coupled “online” chemistry within the WRF model, Atmos. Environ, 39, 6957–6975,
755 <https://doi.org/10.1016/j.atmosenv.2005.04.027>, 2005.

756 Guenther, A., Hewitt, C. N., Erickson, D., Fall, R., Geron, C., Graedel, T., Harley, P., Klinger,
757 L., Lerdau, M., McKay, W. A., Pierce, T., Scholes, B., Steinbrecher, R., Tallamraju, R., Taylor,
758 J., and Zimmerman, P.: A global model of natural volatile organic compound emissions, Journal
759 of Geophysical Research: Atmospheres, 100, 8873–8892, <https://doi.org/10.1029/94JD02950>,
760 1995.

761

762 Hong, S., Noh, Y., and Dudhia, J.: A new vertical diffusion package with an explicit treatment
763 of entrainment processes, Mon. Wea. Rev, 134, 2318–2341,
764 <https://doi.org/10.1175/MWR3199.1>, 2006.

765

766 Huang, X.Y., Xiao, Q., Barker, D. M., Zhang, X., Michalakes, J., Huang, W., Henderson, T.,
767 Bray, J., Chen, Y., Ma, Z., Dudhia, J., Guo, Y., Zhang, X., Won, D., Lin, H., and Kuo, Y.: Four-
768 dimensional variational data assimilation for WRF: Formulation and preliminary results, Mon.
769 Weather Rev, 137, 299–314, <https://doi.org/10.1175/2008MWR2577.1>, 2009.

770



771 Hunt, B. R., Kalnay, E., Kostelich, E. J., Ott, E., Patil, D. J., Sauer, T., Szunyogh, I., Yorke, J.
772 A., and Zimin, A. V.: Four-dimensional ensemble Kalman filtering, *Tellus A: Dynamic*
773 *Meteorology and Oceanography*, 56(4), 273–277, <https://doi.org/10.3402/tellusa.v56i4.14424>,
774 2004.
775
776 Hunt, B. R., Kostelich, E. J., and Szunyogh, I.: Efficient data assimilation for spatiotemporal
777 chaos: a local ensemble transform Kalman filter, *Physica D: Nonlinear Phenomena*, 230, 112–
778 126, <https://doi.org/10.1016/j.physd.2006.11.008>, 2007.
779
780 Iacono, M. J., Delamere, J. S., Mlawer, E. J., Shephard, M. W., Clough, S. A., and Collins, W.
781 D.: Radiative forcing by long-lived greenhouse gases: Calculations with the AER radiative
782 transfer models, *J. Geophys. Res.*, 113, D13103, <https://doi.org/10.1029/2008JD009944>, 2008.
783
784 Jin, J., Pang, M., Segers, A., Han, W., Fang, L., Li, B., Feng, H., Lin, H. X., and Liao, H.:
785 Inverse modeling of the 2021 spring super dust storms in East Asia, *Atmos. Chem. Phys.*, 22,
786 6393–6410, <https://doi.org/10.5194/acp-22-6393-2022>, 2022.
787
788 Kong, L., Tang, X., Zhu, J., Wang, Z., Sun, Y., Fu, P., Gao, M., Wu, H., Lu, M., Wu, Q., Huang,
789 S., Sui, W., Li, J., Pan, X., Wu, L., Akimoto, H., and Carmichael, G. R.: Unbalanced emission
790 reductions of different species and sectors in China during COVID-19 lockdown derived by
791 multi-species surface observation assimilation, *Atmos. Chem. Phys.*, 23, 6217–6240,
792 <https://doi.org/10.5194/acp-23-6217-2023>, 2023.
793



794 Kong, Y., Sheng, L., Li, Y., Zhang, W., Zhou, Y., Wang, W., and Zhao, Y.: Improving PM_{2.5}
795 forecast during haze episodes over China based on a coupled 4D-LETKF and WRF-Chem
796 system, *Atmospheric Research*, 249, 105366, <https://doi.org/10.1016/j.atmosres.2020.105366>,
797 2021.
798
799 Lorenc, A.C.: Analysis methods for numerical weather prediction, *Q. J. R. Meteorol. Soc.*, 112,
800 1177–1194, <https://doi.org/10.1002/qj.49711247414>, 1986.
801
802 Luo, X., Tang, X., Wang, H., Kong, L., Wu, H., Wang, W., SONG, Y., Luo, H., Wang, Y., Zhu,
803 J., and Wang, Z.: Investigating the Changes in Air Pollutant Emissions over the Beijing-Tianjin-
804 Hebei Region in February from 2014 to 2019 through an Inverse Emission Method, *Adv. Atmos.*
805 *Sci.* 40, 601–618, <https://doi.org/10.1007/s00376-022-2039-9>, 2023.
806
807 Ma, C., Wang, T., Jiang, Z., Wu, H., Zhao, M., Zhuang, B., Li, S., Xie, M., Li, M., Liu, J., and
808 Wu, R.: Importance of bias correction in data assimilation of multiple observations over eastern
809 China using WRF-Chem/DART, *Journal of Geophysical Research: Atmospheres*, 125,
810 e2019JD031465, <https://doi.org/10.1029/2019JD031465>, 2020.
811
812 Miyoshi, T., Yamane, S., and Enomoto, T.: Localizing the Error Covariance by Physical
813 Distances within a Local Ensemble Transform Kalman Filter (LETKF), *Scient. Online Lett.*
814 *Atmos.*, 3, 89–92, <https://doi.org/10.2151/sola.2007-023>, 2007.
815



816 Morrison, H., Thompson, G., and Tatarskii, V.: Impact of Cloud Microphysics on the
817 Development of Trailing Stratiform Precipitation in a Simulated Squall Line: Comparison of
818 One- and Two-Moment Schemes, *Mon. Wea. Rev.*, **137**, 991–1007,
819 <https://doi.org/10.1175/2008MWR2556.1>, 2009.
820
821 Miyazaki, K., Eskes, H. J., and Sudo, K.: Global NO_x emission estimates derived from an
822 assimilation of OMI tropospheric NO₂ columns, *Atmos. Chem. Phys.*, **12**, 2263–2288,
823 <https://doi.org/10.5194/acp-12-2263-2012>, 2012a.
824
825 Miyazaki, K., Eskes, H. J., Sudo, K., Takigawa, M., Weele, M. van., and Boersma, K. E.:
826 Simultaneous assimilation of satellite NO₂, O₃, CO, and HNO₃ data for the analysis of
827 tropospheric chemical composition and emissions, *Atmos. Chem. Phys.*, **12**, 9545–9579,
828 <https://doi.org/10.5194/acp-12-9545-2012>, 2012b.
829
830 Miyoshi, T.: LETKF source codes, GitHub, available at: [https://github.com/takemasa-](https://github.com/takemasa-miyoshi/letkf)
831 [miyoshi/letkf](https://github.com/takemasa-miyoshi/letkf), last access: 1 January 2024.
832
833 Ott, E., Hunt, B. R., Szunyogh, I., Zimin, A. V., Kostelich, E. J., Corazza, M., Kalnay, E., Patil,
834 D. J., and Yorke, J. A.: A local ensemble Kalman filter for atmospheric data assimilation. *Tellus*
835 *A*, **56**, 415–428, <https://doi.org/10.1111/j.1600-0870.2004.00076.x>, 2004.
836
837 Pagowski, M., and Grell, G. A.: Experiments with the assimilation of fine aerosols using an
838 ensemble Kalman filter, *Journal of Geophysical Research*, **117**, D21302,
839 <https://doi.org/10.1029/2012JD018333>, 2012.



840

841 Parrish, D. F. and Derber, J. C.: The National Meteorological Center's Spectral Statistical-
842 Interpolation Analysis System, *Mon. Weather Rev.*, 120, 1747–1763,
843 [https://doi.org/10.1175/1520-0493\(1992\)120<1747:TNMCSS>2.0.CO;2](https://doi.org/10.1175/1520-0493(1992)120<1747:TNMCSS>2.0.CO;2), 1992.

844

845 Peng, Z., Liu, Z., Chen, D., and Ban, J.: Improving PM_{2.5} forecast over China by the joint
846 adjustment of initial conditions and source emissions with an ensemble Kalman filter, *Atmos.*
847 *Chem. Phys.*, 17, 4837–4855, <https://doi.org/10.5194/acp-17-4837-2017>, 2017.

848

849 Peng, Z., Lei, L., Liu, Z., Sun, J., Ding, A., Ban, J., Chen, D., Kou, X., and Chu, K.: The impact
850 of multi-species surface chemical observation assimilation on air quality forecasts in China,
851 *Atmos. Chem. Phys.*, 18, 17387–17404, <https://doi.org/10.5194/acp-18-17387-2018>, 2018.

852

853 Rubin, J. I., Reid, J. S., Hansen, J. A., Anderson, J. L., Collins, N., Hoar, T. J., Hogan, T., Lynch,
854 P., McLay, J., Reynolds, C. A., Sessions, W. R., Westphal, D. L., and Zhang, J.: Development
855 of the Ensemble Navy Aerosol Analysis Prediction System (ENAAPS) and its application of
856 the Data Assimilation Research Testbed (DART) in support of aerosol forecasting, *Atmos.*
857 *Chem. Phys.*, 16, 3927–3951, <https://doi.org/10.5194/acp-16-3927-2016>, 2016.

858

859 Schutgens, N. A. J., Miyoshi, T., Takemura, T., and Nakajima, T.: Sensitivity tests for an
860 ensemble Kalman filter for aerosol assimilation, *Atmos. Chem. Phys.*, 10, 6583–6600,
861 <https://doi.org/10.5194/acp-10-6583-2010>, 2010.



862

863 Sun, W., Liu, Z., Chen, D., Zhao, P., and Chen, M.: Development and application of the
864 WRFDA-Chem three-dimensional variational (3DVAR) system: aiming to improve air quality
865 forecasting and diagnose model deficiencies, *Atmos. Chem. Phys.*, 20, 9311–9329,
866 <https://doi.org/10.5194/acp-20-9311-2020>, 2020.

867

868 Schwartz, C. S., Liu, Z., Lin, H. C., and McKeen, S. A.: Simultaneous three-dimensional
869 variational assimilation of surface fine particulate matter and MODIS aerosol optical depth, *J.*
870 *Geophys. Res.*, 117, D13202, <https://doi.org/10.1029/2011JD017383>, 2012.

871

872 Stockwell, W. R., Kirchner, F., Kuhn, M., and Seefeld, S.: A new mechanism for regional
873 atmospheric chemistry modeling, *J. Geophys. Res.*, 102, 25847–25879,
874 <https://doi.org/10.1029/97JD00849>, 1997.

875

876 Tewari, M., Chen, F., Wang, W., Dudhia, J., LeMone, M. A., Mitchell, K., Ek, M., Gayno, G.,
877 Wegiel, J., and Cuenca, R. H.: Implementation and verification of the unified NOAH land
878 surface model in the WRF model, 20th conference on weather analysis and forecasting/16th
879 conference on numerical weather prediction, pp. 11–15, 2004.

880

881 van Donkelaar, A., Martin, R. V., Brauer, M., Hsu, N. C., Kahn, R. A., Levy, R. C., Lyapustin,
882 A., Sayer, A. M., and Winker, D. M.: Global estimates of fine particulate matter using a
883 combined geophysical-statistical method with information from satellites, models, and



884 monitors, *Environ. Sci. Technol*, 50, 3762–3772, <https://doi.org/10.1021/acs.est.5b05833>, 2016.

885

886 Wang, Z., Li, J., Wang, Z., Yang, W., Tang, X., Ge, B., Yan, P., Zhu, L., Chen, X., and Chen, H.:

887 Modeling study of regional severe hazes over mid-eastern China in January 2013 and its

888 implications on pollution prevention and control, *Sci. China-Earth Sci.*, 57, 3–13,

889 <https://doi.org/10.1007/s11430-013-4793-0>, 2014.

890

891 Whitaker, J. S. and Hamill, T. M.: Ensemble data assimilation without perturbed observations,

892 *Mon. Weather Rev.*, 130, 1913–1924, <https://doi.org/10.1175/1520->

893 0493(2002)130<1913:EDAWPO>2.0.CO;2, 2002.

894

895 Yan, S., Cao, H., Chen, Y., Wu, C., and Fan, H.: Spatial and temporal characteristics of air

896 quality and air pollutants in 2013 in Beijing, *Environ Sci Pollut Res.*, 23, 13996–14007,

897 <https://doi.org/10.1007/s11356-016-6518-3>, 2016.

898

899 Yumimoto, K., and Takemura, T.: Direct radiative effect of aerosols estimated using ensemble-

900 based data assimilation in a global aerosol climate model, *Geophysical Research Letters*, 38,

901 L21802, <https://doi.org/10.1029/2011GL049258>, 2011.

902

903 Zheng, B., Cheng, J., Geng, G., Wang, X., Li, M., Shi, Q., Qi, J., Lei, Y., Zhang, Q., He, K.:

904 Mapping anthropogenic emissions in China at 1 km spatial resolution and its application in air

905 quality modeling, *Science Bulletin*, 66(6), 612-620, <https://doi.org/10.1016/j.scib.2020.12.008>,



906 2021.

907

908 Zhang, L., Li, Q., Wang, T., Ahmadov, R., Zhang, Q., Li, M., and Lv, M.: Combined impacts
909 of nitrous acid and nitryl chloride on lower-tropospheric ozone: new module development in
910 WRF-Chem and application to China, *Atmos. Chem. Phys.*, 17, 9733–9750,
911 <https://doi.org/10.5194/acp-17-9733-2017>, 2017.

912

913 Zhang, Q., Streets, D. G., Carmichael, G. R., He, K. B., Huo, H., Kannari, A., Klimont, Z., Park,
914 I. S., Reddy, S., Fu, J. S., Chen, D., Duan, L., Lei, Y., Wang, L. T., and Yao, Z. L.: Asian
915 emissions in 2006 for the NASA INTEX-B mission, *Atmos. Chem. Phys.*, 9, 5131–5153,
916 <https://doi.org/10.5194/acp-9-5131-2009>, 2009.

917

918 Zhao, Y., Greybush, S. J., Wilson, R. J., Hoffman, R. N., and Kalnay, E.: Impact of assimilation
919 window length on diurnal features in a Mars atmospheric analysis, *Tellus A*, 67, 26042,
920 <https://doi.org/10.3402/tellusa.v67.26042>, 2015.

921

922 Zhang, Q., Ma, Q., Zhao, B., Liu, X., Wang, Y., Jia, B., and Zhang, X.: Winter haze over North
923 China Plain from 2009 to 2016: Influence of emission and meteorology, *Environmental*
924 *Pollution*, 242(B), 1308–1318, <https://doi.org/10.1016/j.envpol.2018.08.019>, 2018.

925